Effect of Ultrasonic Capillary Dynamics on the Mechanics of Thermosonic Ball Bonding

Yan Huang, Aashish Shah, Michael Mayer, Norman (Y.) Zhou, and John Persic

***Abstract*—Microelectronic wire bonding is an essential step in today's microchip production. It is used to weld (bond) microwires to metallized pads of integrated circuits using ultrasound with hundreds of thousands of vibration cycles. Thermosonic ball bonding is the most popular variant of the wire bonding process and frequently investigated using finite element (FE) models that simplify the ultrasonic dynamics of the process with static or quasistatic boundary conditions. In this study, the ultrasonic dynamics of the bonding tool (capillary), made from Al_2O_3, is included in a FE model. For more accuracy of the FE model, the main material parameters are measured. The density of the capillary was measured to be $\rho_{cap} = 3552 \pm 100$ kg/m^3. The elastic modulus of the capillary, $E_{cap} = 389 \pm 11$ GPa, is found by comparing an auxiliary FE model of the free vibrating capillary with measured values. A capillary "nodding effect" is identified and found to be essential when describing the ultrasonic vibration shape. A main FE model builds on these results and adds bonded ball, pad, chip, and die attach components. There is excellent agreement between the main model and the ultrasonic force measured at the interface on a test chip with stress microsensors. Bonded ball and underpad stress results are reported. When adjusted to the same ultrasonic force, a simplified model without ultrasonic dynamics and with an infinitely stiff capillary tip is substantially off target by −40% for the maximum underpad stress. The compliance of the capillary causes a substantial inclination effect at the bonding interface between wire and pad. This oscillating inclination effect massively influences the stress fields under the pad and is studied in more detail. For more accurate results, it is therefore recommended to include ultrasonic dynamics of the bonding tool in mechanical FE models of wire bonding.**

I. Introduction

Thermosonic wire bonding is the most preferred method for electrical connections to ICs [1]. In this process, a microwire loop is welded to a metallization pad of an IC and to a substrate terminal, thereby interconnecting the IC with a larger scale substrate circuit. Welding (bonding) of the wire to the IC is achieved by a combination of constant normal force F_N, pressing the wire to the pad, and an ultrasonic force $F_{US}(t) = F_{US} \sin(2\pi f t)$, where f is the ultrasonic frequency and t is the time. The forces produce sliding friction at the contact zone between wire and pad (interface). This leads to some wear (cleaning) and then to the bond being established.

The industry is continuously looking for methods to reduce the cost and improve the performance and speed of the process. One approach toward these goals is to avoid bond failure such as underpad damage that is connected to the high underpad stress caused by the normal and ultrasonic forces required for successful ball bonding. Another effect of high bonding stress is localized pad thinning [2], which leads to higher underpad stress and degradation of the bond reliability. Underpad damage can occur as delamination of layers, bond pad peel off, fracture of dielectrics or underpad interfaces, or Si cratering as illustrated in Figs. 1(a)–(c), respectively.

Finite element analysis (FEA) is an excellent way to obtain insight into physical quantities highly localized to the contact zone (bond interface). The ball bonding process includes several physical mechanisms that have been partly described by FE models, for example, plastic wire deformation [3]–[11], work hardening and/or rate-dependent properties of wire or pad [6]–[12], interfacial friction [3], [6], [7], [9], [10], [13], ultrasound (US) cycles [3], [4], [6], [9], [11], [13], cyclic plasticity [14], dynamic effects of the bonding tool (capillary) [4], [15], and thermal effects [7], [9]. Process factors studied are bond force and US-related parameters [3], [7], [9], US frequency [7], friction coefficient [6], [7], mechanical properties [6], [8], wire/pad dimensions [7], [8], and shape of tool tip [8]. Responses investigated were underpad stress [3], [4], [6], [7], [9], interfacial friction [3], wire stress/shape [4], [7]–[9], plastic dissipation energy [6], [7], residual stress [9], and temperature [7].

In particular, Takahashi and Inoue [8] report a 2-D FEA ball-bond model to analyze the behavior of the interfacial plastic deformation with change in pad thickness, pad hardness, and tool tip shape. Directional effects of US are excluded. Guidelines are given how to change the pad and tool geometry to influence the distribution of pad and wire plastic extension and to facilitate homogeneous bonding over the interface. Viswanath *et al.* [6] report a 2-D FEA ball-bond model and describe the interfacial deformation of the bond pad with changes in parameters such as friction coefficient and pad properties. Increasing the pad metallization thickness and hardness can minimize the von Mises stress under the pad. The study excludes dynamic capillary effects. Zhang *et al.* [3] report the stress distribution for various bond-pad thicknesses and the levels of overall friction. A 3^2 full factorial design of experiment is reported with varying bond force (F_N) and US amplitude (A_{US}). No other factors were varied, and dynamic capillary effects were excluded.

Manuscript received July 2, 2009; accepted October 2, 2009. This work is supported by the Natural Sciences and Engineering Research Council (NSERC) of Canada, the Initiative for Automotive Manufacturing Innovation (IAMI) of Ontario (Canada), and the Ontario Centres of Excellence (OCE), Microbonds Inc. (Markham, Canada), and MK Electron Co. Ltd. (Yongin, Korea).

Y. Huang, A. Shah, M. Mayer, and N. Zhou are with the Center of Advanced Materials Joining, University of Waterloo, Waterloo, Ontario, Canada (e-mail: ashah011@engmail.uwaterloo.ca).

J. Persic is with Microbonds Inc., Research and Development Department, Markham, Ontario, Canada.

Digital Object Identifier 10.1109/TUFFC.2010.1402

0885–3010/$25.00 © 2010 IEEE

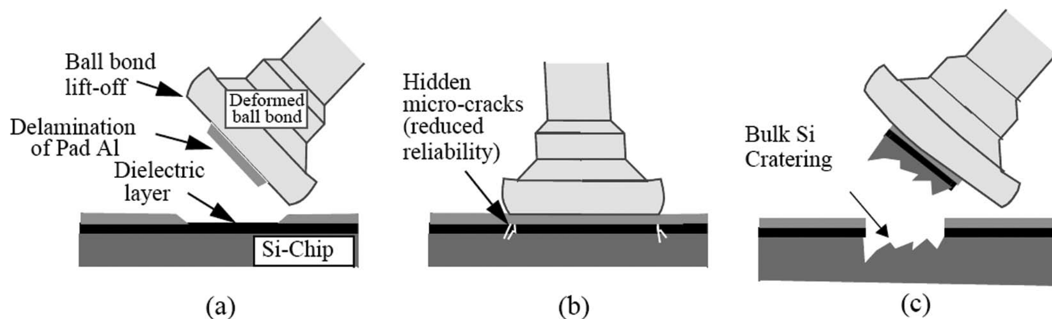

Fig. 1. Illustration of underpad damage types: (a) bond pad peel off, (b) hidden microcracks, and (c) bulk Si cratering.

Previous studies covered either the dynamic ultrasonic behavior of the capillary or the ultrasonic stresses in the bonded wire and underpad structures. However, the authors are not aware of any report on a combination of these 2 types of studies. Therefore, it is worthwhile to investigate the ultrasonic dynamics of the capillary because they possibly dominate the form of the stress fields. In this contribution, FE models are established that describe the influences of the capillary vibration dynamics on stress fields and on the US force F_{US} acting on (parallel to) the interface.

II. Ball Bonding Process

The major process factors in ball bonding are F_{N}, A_{US}, and the way these factors are controlled over time. These factors determine the 2 major mechanisms observed in the thermosonic ball bonding process, which are the plastic deformation of the free-air ball (FAB) and the bond formation at the interface.

The present study is confined to a double-stage bond-force process [16], [17], which is characterized by a relatively high impact force to bond force ratio causing most or all of the ball deformation already before US starts. During the subsequent US period, the bond forms uniformly over the interface. This allows for more uniform bonded-ball geometries, faster throughput due to faster search/approach times (i.e., higher contact velocities), and potentially more reliable bonds because of more uniform intermetallic coverage formed at the interface.

The bond formation phase starts with ultrasonic dissipation, during which the ball performs a harmonically forced stick-slip oscillation [18], similar to that reported by [19], transmitting friction force to the chip. The friction energy and wear causes the formation of microwelds that grow in size until they cover most of the interface. The more microwelds, the more ultrasonic force is transmitted to the chip. Consequently, maximum force and maximum underpad stresses are expected at the end of the bond formation phase just before the ultrasonic dissipation is switched off. This study focuses on those stresses and the UPD risk caused by them.

III. Numerical

The FE software suite COMSOL 3.4 is used. The model geometries extend in 3 dimensions in a Cartesian coordinate system and include a standard capillary that is suitable for an 80-μm bond pad pitch process. First, model assumptions, boundary conditions, and material parameters are discussed. Second, an auxiliary model (model $\mathrm{U}_{\mathrm{free}}$) is introduced to determine a missing capillary parameter using a comparison with previously reported experimental data. Last, the ultrasonic model of the bonded ball (model $\mathrm{U}_{\mathrm{dynamic}}$) is presented and validated by comparison with experimental results.

A. Assumptions and Boundary Conditions

Ultrasound is included in the model using a frequency analysis (sometimes called harmonic response analysis), giving a nontransient, steady-state response of the ultrasonic oscillation forced onto the system. Other simplifying assumptions are

1. No plastic deformation. The ball is predeformed, i.e., in its final shape as after the bond.
2. No thermal effects.
3. No interfacial friction. Perfect mechanical connections are assumed at the ball-chip and ball-capillary contact zones.
4. Intermetallic growth and any other bond formation effects are ignored.
5. Effects of air-damping on the capillary vibration are assumed negligible.

This geometry neither includes the ultrasonic horn nor the transducer nor the capillary portion clamped by the transducer. Only the capillary part protruding from the horn is simulated. The top surface area (TSA) of that part is where the ultrasonic boundary condition is applied. The z-direction is the main capillary direction and perpendicular to the chip surface. The ultrasonic vibration is applied in y-direction and is assumed symmetrical with respect to x. Therefore, only the $x \geq 0$ half of the geometry is modeled for simplicity.

The notation used in this paper is provided in Table I.

TABLE I. NOTATION.

Symbol	Description
F_N	Nominal (applied) bond force (normal force)
F_{US}	Ultrasonic force at ball/pad interface
L_{US}	Optimized ultrasonic parameter level
A_{US}	Ultrasonic amplitude
A_{US}^{Hfree}	Ultrasonic amplitude of horn tip in free-air vibrating mode
A_{US}^{Hbond}	Ultrasonic amplitude of horn tip during bonding process
A_{tip}	Ultrasonic amplitude of capillary tip
A_{node}^{exp}	Ultrasonic amplitude of the node
z_{node}	Location of the node measured from capillary tip
ρ_{cap}	Mass density of capillary material
E_{cap}	Elastic modulus of capillary material
ν_{cap}	Poissons ratio
η	Loss factor during viscous damping
TLE	Length of the capillary tool extending from the horn
TSA	Top surface area of capillary tool
TBBS	Typical bonded ball bulk stress
IFA	Interfacial area of bonded ball
δ_z	Ultrasonic displacement of TSA during horn nodding
ε	Nodding angle
F_N^{exp}	Measured (actual) bond force
F_1	First harmonic of the microsensor force signal
F_{US}^{exp}	Measured ultrasonic force at the ball/pad interface
F_{US}^{sim}	Simulated ultrasonic force at the ball/pad interface
τ_{yz}^{US}	Shear stress component contributing to F_{US}^{sim}
σ_z	Stress component in z direction
σ_z^N	Normal force component of the z stress
σ_z^{US}	Ultrasound component of the z stress
P_z	Pressure applied at TSA in z direction due to F_N
σ_Y	Stress component in y direction
σ_{VM}	von Mises stress
σ_t	Uniaxial tensile yield stress limit
σ_c	Uniaxial compressive yield stress limit
$\sigma_1, \sigma_2, \sigma_3$	Principal stress components
σ_{max}	Simulated combined maximum principal stress
σ_{min}	Simulated combined minimum principal stress
l_t	Line fraction of the tensile zone

B. Material Parameters

The materials for the components are those commonly used in the industry: microcrystalline Al_2O_3 for the capillary, Au for the deformed ball, Si for the chip, and cured Ag-filled epoxy for the adhesive. The material properties required for a frequency analysis are the elastic modulus, Poisson ratio, mass density, and damping coefficient. The capillary material properties mass density ρ_{cap} and elastic modulus E_{cap} have a major effect on the ultrasonic model. Therefore, ρ_{cap} is measured using a buoyancy-based method. A penetrating oil with known density was used that readily creeps into the capillary tip holes. The experiment was constraint to a minimum sample mass, which was reached when using 4 capillaries per measurement. Thus, 32 capillaries were used in 8 groups to obtain 8 measurements of ρ_{cap}. The resulting average mass density ± standard deviation is

$$\rho_{cap} = 3552 \pm 100 \text{ kg/m}^3. \tag{1}$$

The value of E_{cap} for alumina at room temperature depends on the grain size and porosity and ranges from about 310 to 450 GPa [20]–[23]. The value used for the simulation models in this work is determined in a later subsection. The loss factor (or internal friction Q^{-1} [24]) for viscous damping is estimated to be

$$\eta = 2 \times 10^{-4} \tag{2}$$

from the room temperature data in [21], [25]. The Poisson ratio of low porosity alumina is estimated from [23], $\nu_{cap} = 0.25$.

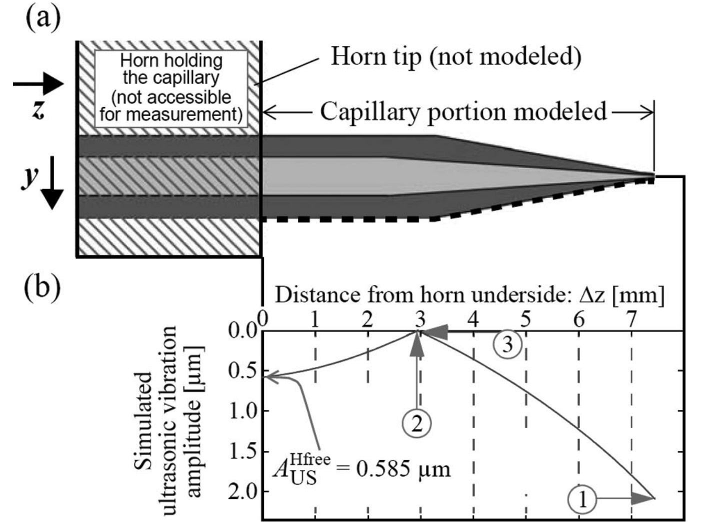

Fig. 2. Model U_{free} adjusted to measurement. (a) Cross-sectional shape of capillary used; vibration measurement along dashed line. (b) Simulated vibration amplitude, adjusted to measured conditions ⟨1⟩–⟨3⟩ (3); Frequency = 130 kHz.

C. Ultrasonic Model of Free Capillary (U_{free})

By adjusting the model described in this section to experimental data, 2 missing parameters for the capillary vibration can be determined.

1) Experimental: The ultrasonic vibration shape (amplitude A_y^{exp}) of a typical capillary in free vibration with a frequency of 130 kHz was measured with a laser vibrometer moved in z-direction along the continuously vibrating capillary shown in Fig. 2(a) and reported in chapter 3 of [4]. The vibration has one node located close to the middle of the capillary part protruding from the horn. The vibration was driven by a horn amplitude of $A_{US}^{Hfree} = 0.585$ µm acting on TSA.

Three characteristic quantities for the vibration shape are extracted from the results in [4]. They concern the tip amplitude A_{tip}, the node location z_{node} (measured from the tip), and the amplitude at the node A_{node}^{exp}:

$$\left.\begin{array}{ll} \langle 1\rangle & A_{tip} = 2.07 \ \mu\text{m} \\ \langle 2\rangle & z_{node} = -4.6 \text{ mm} \\ \langle 3\rangle & A_{node}^{exp} < 10 \text{ nm} \end{array}\right\}. \tag{3}$$

These characteristics are used as 3 conditions to which the FE model U_{free} is adjusted.

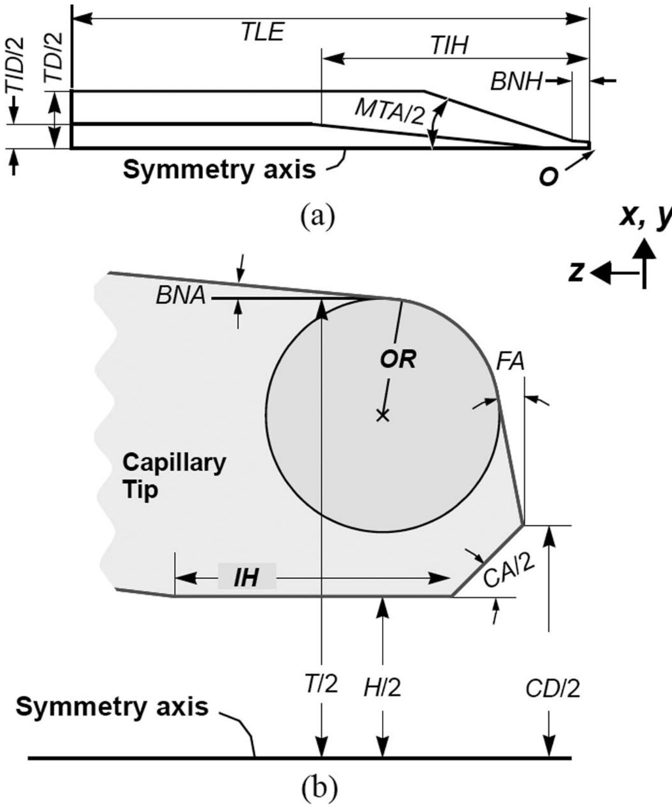

Fig. 3. Layout of capillary model with parameter definitions. Only half of geometry shown (for symmetry): (a) overall and (b) tip detail.

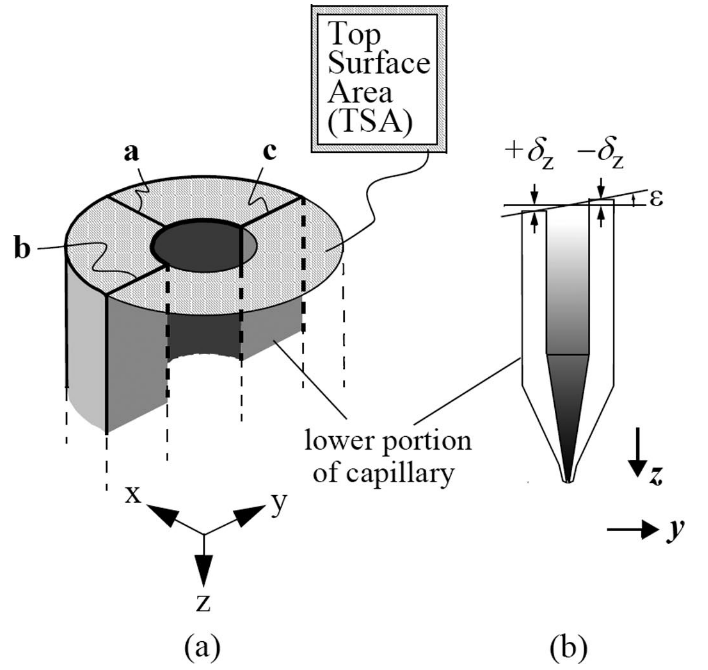

Fig. 4. (a) Definition of straights **a** ($y = 0$), **b** ($x = 0$), **c** ($x = 0$), and TSA. (b) Approximate implementation of capillary boundary conditions for horn nodding, oscillating from plus to minus with ultrasonic frequency.

TABLE II. FE Model Geometry Values.

Quantity	Variable	Value
Bottle neck angle	BNA [°]	10
Bottle neck height	BNH [μm]	275
Chamfer angle	CA [°]	90
Chamfer diameter	CD [μm]	50
Face angle	FA [°]	11
Hole diameter	H [μm]	38
Inner height	IH [μm]	42
Outside radius	OR [μm]	12
Tool outer diameter	TOD [μm]	1587
Tool inner diameter	TID [μm]	600
Tool inner height	TIH [μm]	4875
Tool length extending	TLE [μm]	7600
Tool main taper angle	MTA [°]	20

2) Model Definitions and Horn Nodding Effect: Although the total height for the capillary is 11.1 mm, only the length of the capillary tool extending from the horn (TLE) is modeled. Capillary geometry parameters used in both experiment and simulation are given in Table II and illustrated in Figs. 3(a) and (b). The FE model uses ultrasonic displacement $A_{\mathrm{US}}^{\mathrm{Hfree}}$ in y-direction at TSA as its main boundary condition. The material parameters are those given previously with the exception of E_{cap}, the value of which is determined by adjusting the simulated vibration shape shown in Fig. 2(b) to the experimental values in (3).

However, the experimental match cannot be found by varying E_{cap} alone. Therefore, the rotational compliance effect [4] is implemented and adjusted, too. The rotational compliance reflects the limited stiffness of the horn holding the capillary. The capillary moment acts on the horn. This causes a minute "horn nodding" effect. It is modeled with an additional set of boundary conditions that describe a nodding oscillation of the TSA. The way this boundary condition is implemented is described using Figs. 4(a) and (b). Fig. 4(a) defines the straight lines **a**, **b**, and **c**. An angle ε is defined as shown in Fig. 4(b) describing the TSA nodding. The effect of ε is approximated by ultrasonic displacement conditions $+\delta_z$ and $-\delta_z$ at lines **b** and **c**, respectively, where

$$\delta_z = \tan(\varepsilon) \times (\mathrm{TD} - \mathrm{TID}) \times 0.25 \quad (4)$$

and TD and TID are given in Table II. To stabilize the model, the line **a** on TSA is held fixed in z-direction.

3) Determination of tan(ε) and E_{cap}: A total of 289 combinations of E_{cap} and ρ_{cap} test values are evenly taken from the ranges 300 to 460 GPa and 3500 to 3900 kg m^{-3}, respectively, to test the conditions in (3) numerically. Condition ⟨3⟩ is fulfilled for all the combinations if $\eta < 2.8 \times 10^{-2}$. Conditions ⟨1⟩ and ⟨2⟩ are fulfilled simultaneously if and only if

$$E_{\mathrm{cap}} = 0.1121\ [\mathrm{GPa\ kg^{-1}\ m^3}] \times \rho_{\mathrm{cap}} - 12.56\ [\mathrm{GPa}] \quad (5)$$

and

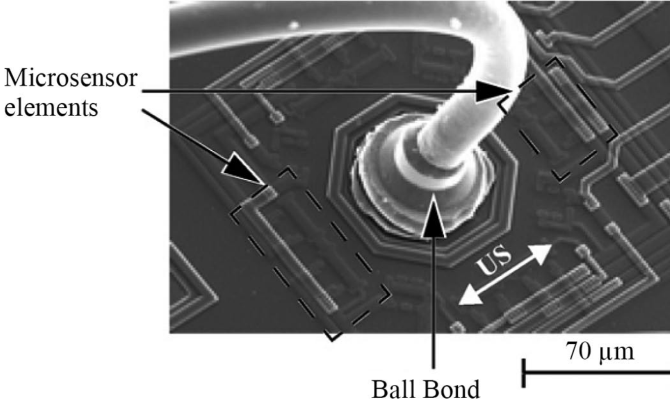

Fig. 5. SEM image of the microsensor setup [26].

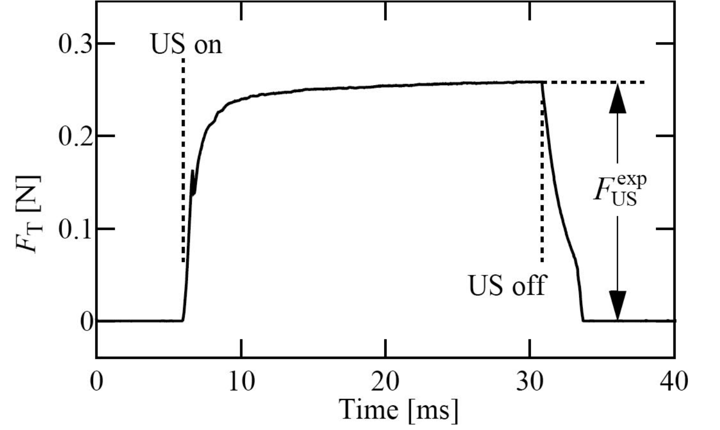

Fig. 6. Amplitude of fundamental harmonic of the ultrasonic force in y-direction measured during ball bonding (derived from [29], [30]).

$$\tan(\varepsilon) = -4.179 \times 10^{-11}\ [\mathrm{kg^{-1}\ m^3}] \times \rho_{cap} - 5.617 \times 10^{-5}. \quad (6)$$

Thus, the value of ε is $-0.0032°$. Using (1), (4), and (6) with values from Table II, the boundary condition value

$$\delta_z = -13.896 \pm 0.001\ \mathrm{nm} \quad (7)$$

is found. Finally, with (1) and (5),

$$E_{cap} = 389 \pm 11\ \mathrm{GPa} \quad (8)$$

is found. This elastic modulus is within the range of published values for alumina with low porosity [23].

D. Ultrasound Model of Bonded Ball ($U_{dynamic}$)

1) Experimental: Bonding experiments are carried out on a microsensor test chip and described in [26]. They are carried out in a different laboratory than the experiments used for the free capillary vibration. The wire bonder is of the same type but has a slightly lower ultrasonic frequency. The capillary used is made from the same material but has a different geometry.

The bonding experiments are briefly summarized here. For bonding a Au ball with a bond time of 25 ms, impact force of 588 mN, and typical measured bond force of $F_N^{exp} = 236$ mN, an optimized US parameter level is $L_{US} = 42\%$ and is proportional to the ultrasonic amplitude of the horn tip. The conversion formula used [27] is A_{US}^{horn} [μm] = L_{US} [%] × 0.0133 [μm/%]. Thus, L_{US} converts to the ultrasonic amplitude at the horn tip

$$A_{US}^{Hbond} = 0.559\ \mu\mathrm{m}. \quad (9)$$

This value is the same for the free vibration and the bonded ball case, a feature provided by the constant current amplitude delivered to the transducer on this wire bonder. An updated transducer was used that has an US frequency of $f = 128$ kHz. A resulting ball bonded with optimized parameters on the test pad in between the microsensor elements is shown in Fig. 5. On average, this process results in ball heights of 16.3 μm, ball diameters of 59.4 μm (measured at the capillary imprint), and shear strength of 119 MPa.

The microsensor on the test chip that was used for this experiment measures the interfacial US force. It consists of 4 piezoresistive elements (p^+-diffusions of the CMOS process) placed next to the test pad in a Wheatstone bridge configuration. During ball bonding, the change in stress is converted into a change in relative resistance expressed as a differential voltage signal divided by the bridge supply voltage [4], [28]. This microsensor signal is postprocessed (filtered) to obtain the 1st harmonic amplitude, F_1, of the experimental US force transmitted to the bonding pad in y-direction and shown in Fig. 6. The filtering discards lower frequency parasitic vibrations. For a series of ball bonds, the average maximum value (±standard deviation) of F_1 is [26], [29], [30]

$$F_{US}^{exp} = 258 \pm 0.016\ \mathrm{mN}, \quad (10)$$

which is equivalent to an average shear force of 98 MPa at the interface. In the next section, FE models are presented to simulate a value F_{US}^{sim} that is an equivalent to F_{US}^{exp}.

2) Model Definitions: The capillary used in model $U_{dynamic}$ is that used for the experiments [26]. In contrast to the geometry of model U_{free}, it has a tip hole diameter of $H_{fixed} = 35$ μm and its main taper angle MTA is 30°. All other parameters are the same (Table II). Additional model geometries include a bonded ball, chip with pad structure, and die attach material, similar to those in [31].

Geometry parameters are given in Table III and are illustrated in Fig. 7. The chip measures 2 × 2 mm and is 500-μm thick. The adhesive layer has the same horizontal extension and is 50-μm thick. The pad structure consists of a metallization layer that is embedded in a typical CMOS dielectric layer stack treated here as one uniform component (dielectric). On the upper side of the pad metallization, there is a window through the dielectric allowing for bonding (pad opening). The modeled pad

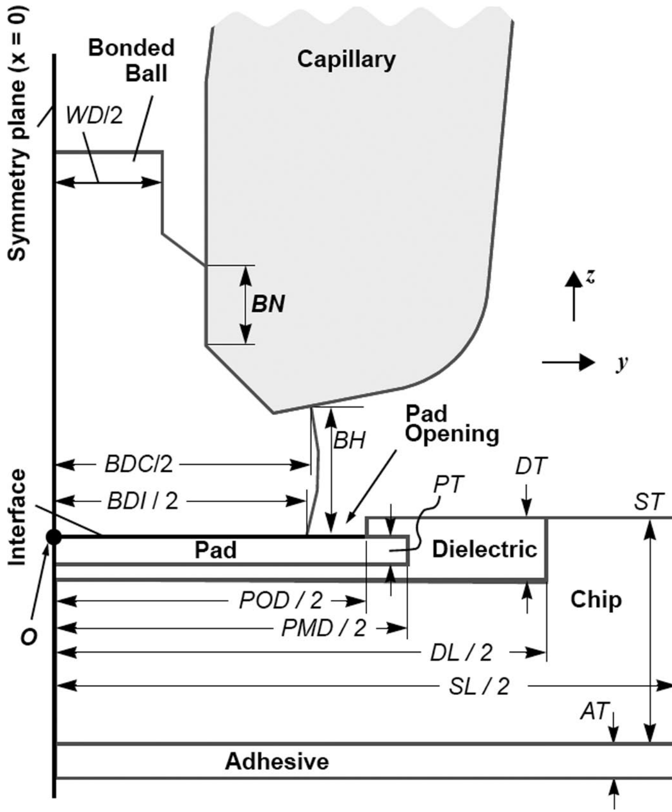

Fig. 7. Layout of model; ball bond detail; not to scale.

TABLE III. FE Model Geometry Values for Ball, Chip with Pad Structure, and Adhesive.

Quantity	Variable	Value [µm]
Ball ∅ at capillary	BDC	59.4
Ball ∅ at interface	BDI	58
Ball height	BH	16.3
Ball neck height	BN	10
Adhesive thickness	AT	50
Silicon length	Sl	2000
Silicon thickness	ST	500
Wire diameter	WD	25
Pad thickness	PT	2
Pad opening ∅ (min.)	POD	70
Pad metallization ∅ (min.)	PMD	75
Dielectric thickness	DT	4
Dielectric layer length	DL	150

metallization and pad opening have octahedral shapes like the pad in Fig. 5. The interfacial area IFA is defined by IFA = π BDI $^2/4$ = 2624 µm^2, where BDI is the ball diameter at the interface (Table III). The origin O with coordinates $(0, 0, 0)$ is located at the interface center shown in Fig. 7 and is 300 µm from the closest chip edge in positive y-direction.

The mesh used is shown in Figs. 8 and 9 for the ball bond detail and the whole geometry, respectively. Maximum mesh element sizes down to 0.2 µm are set for several lines of interest in the ball bond region. All other regions are meshed more coarsely. The mesh elements are

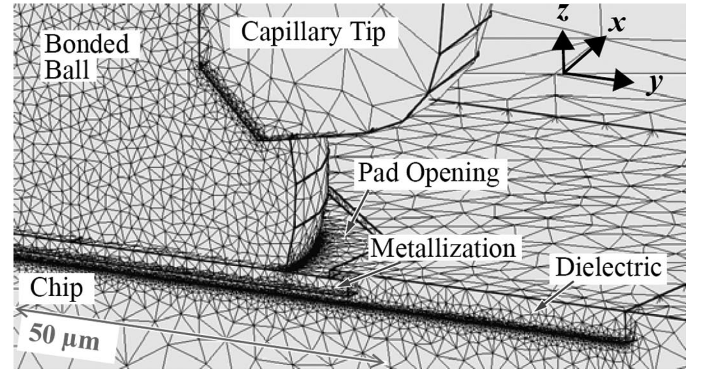

Fig. 8. Mesh detail including ball bond portion of model.

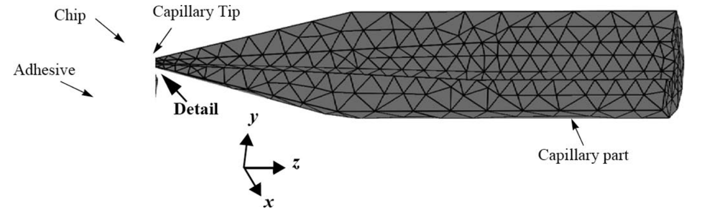

Fig. 9. Mesh of entire model. Only half of entire geometry is modeled. Only part of capillary is modeled.

tetrahedral and their total number is 96 284 resulting in 440 670 degrees of freedom.

Boundary conditions similar to those of model U_{free} are used. The ultrasonic displacement of A_{US}^{Hbond} (9) and δ_z (7) are applied to TSA. The bottom of the adhesive layer is kept fixed as illustrated in Fig. 10(a). The US frequency is the same as in the experiment.

Material parameters other than those given for the capillary earlier are given in Table IV. The Si chip is simplified as an isotropic component.

3) Validation of Ultrasonic Force at Interface: After the simulation calculation is finished, the stress and deformation information for all modeled components is available for any phase of the ultrasonic cycle. From this information, the simulated ultrasonic force amplitude at the interface is deducted,

$$F_{US}^{sim} = \int \tau_{yz}^{US} \mathrm{dIFA} = 251 \text{ mN}, \quad (11)$$

where τ_{yz}^{US} is the only US stress component contributing to F_{US}, and the integration is carried out over IFA. The numerical (11) and experimental (10) values for F_{US} are not significantly different from each other. The simulated value F_{US}^{sim} is 2.7% lower than the experimental average value (10), a difference that is within the experimental error (4.3%). Uncertainties of geometrical dimensions, process settings, and material properties can have substantial influence on the error of F_{US}^{sim}. For example, if replacing ρ_{cap} and E_{cap} by $\rho_{cap} + \sigma$ and $E_{cap} + \sigma$ (σ = standard deviation) as defined in (1) and (8), respectively, F_{US}^{sim} changes by +2.5%. A more detailed sensitivity anal-

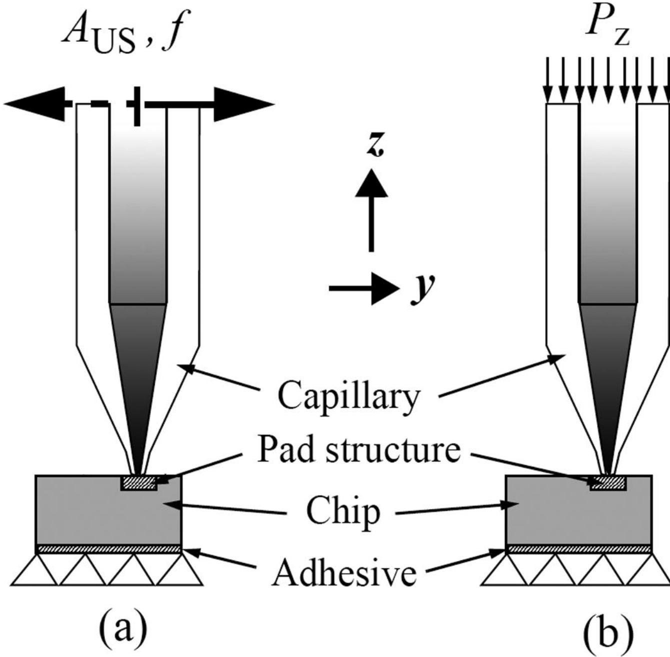

Fig. 10. Main boundary conditions for (a) ultrasound (displacement amplitudes, frequency) and (b) bond force F_N (static pressure). Adhesive bottom fixed for both models; not to scale.

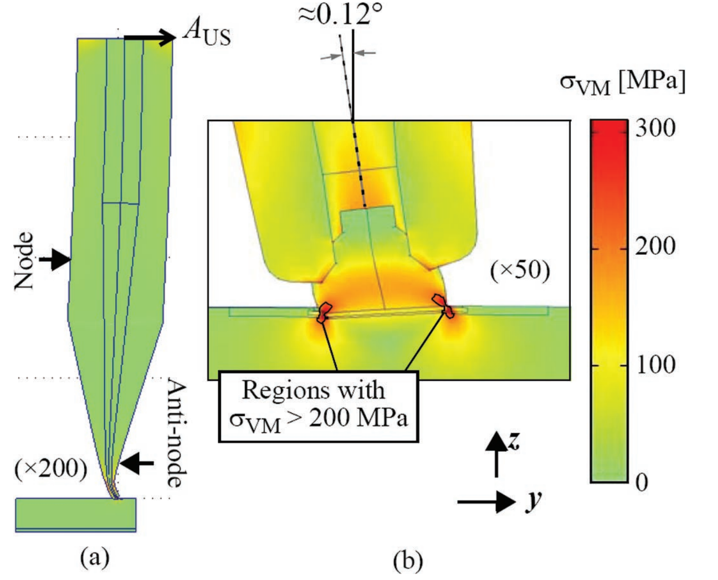

Fig. 11. Ultrasonic von Mises stress σVM and deformation required for F_{US}^{sim} = 258 mN: (a) whole model and (b) bonded ball detail. Ultrasonic frequency = 128 kHz. F_N effect is excluded; deformation not to scale.

ysis of input variable changes will be helpful for future studies.

4) Ultrasonic Vibration Shape and Oscillation Gaps: The state of maximum deformation during the ultrasonic cycle is shown in Figs. 11(a) and (b) for the whole model (scale factor 200) and the bonded ball detail (scale factor 50), respectively. The effect of F_N is excluded in these results. There is one vibration node at z = 3930 μm, and one vibration antinode at z = 554 μm. The capillary tip is considerably inclined (≈ 0.12°) with respect to the z direction.

This capillary tip inclination changes the uniformity of the interfacial σ_z stress produced by the bonding force ("inclination effect"). Although F_N provides a mainly constant σ_z^N at the interface to allow for an uniform bonding process, the inclination oscillation adds an ultrasonically oscillating component σ_z^{US} to the z stress, $\sigma_z = \sigma_z^N + \sigma_z^{US}$. As the inclination oscillation is nonconstant, its effect is recommended to be below a certain limit for practical applications. The inclination oscillation might cause tensile values of σ_z to exist during a fraction of an ultrasonic cycle at the side opposite to the momentary US direction of the capillary tip. Most of this tensile σ_z^{US} stress is compensated in the real bonding process by the compressive σ_z^N. To visualize this compensation, a basic bond force FE model with F_N = 230 mN (value taken from the experiment) is developed. The effect of F_N is produced using a pressure $P_z = F_N/\mathrm{TSA}$ = 137.1 kPa, as shown in Fig. 10(b), where

$$\mathrm{TSA} = \pi \cdot (\mathrm{TD}^2 - \mathrm{TID}^2)/4 = 1.678\ \mathrm{mm}^2 \tag{12}$$

is the (complete) capillary top surface area. The stress σ_z^N is calculated right under IFA at $z = -0.1$ μm. The total stress $\sigma_z = \sigma_z^N + \sigma_z^{US}$ is shown in Fig. 12(a) and with its components in Fig. 12(b). The simulation predicts a "tensile zone" for σ_z extending across ≈ 22% of IFA and indicated by cross hatch in Figs. 12(a) and (b). Along the $x = 0$ line of the interface, the line fraction l_t where σ_z is tensile, is l_t = 0.23.

In the beginning of real bonding, tensile σ_z is expected to initially produce tiny, oscillating gaps on the $+y$ and $-y$ sides, as illustrated in Fig. 13(a) for the $-y$ case. This gap is expected to disappear because it is bonded with the help of the compressive σ_z of the alternate half cycles. Once bonding is strong enough to prevent the gap from reopening, another gap is expected to form at the capillary chamfer above the initial gap location, between capillary

TABLE IV. Material Parameters for Ball, Chip With Pad Structure, and Adhesive [26].

Component	Material	E [GPa]	ρ [kg m^{-3}]	v [–]
Bonded ball	Au	77.2	19 290	0.424
Pad	Al	70	2700	0.35
Dielectric	SiO_2	70	2200	0.17
Adhesive	Epoxy	5	920	0.33
Chip	Si	170	2329	0.28

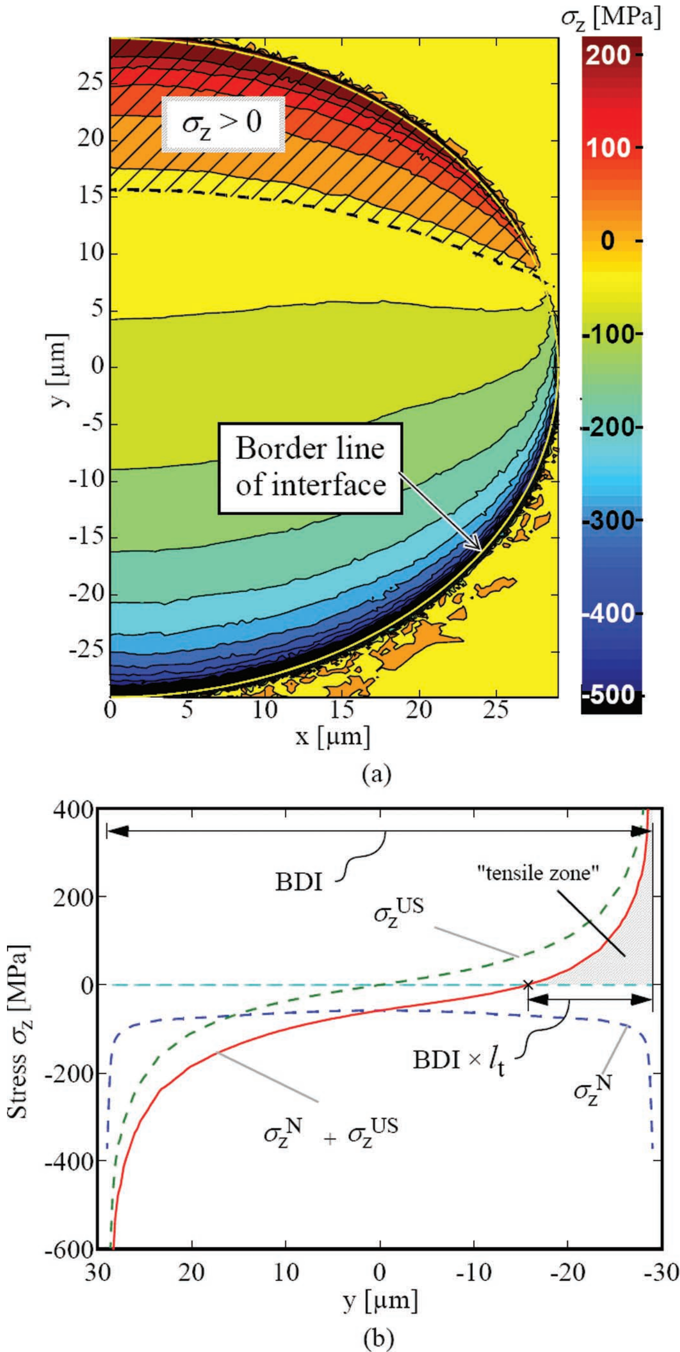

Fig. 12. Stress component σ_z at location under IFA ($z = -0.1$ μm): (a) top view and (b) on-symmetry plane for ultrasound case, bondforce case, and combined case ($x = 0$). Cross hatch indicates tensile zone.

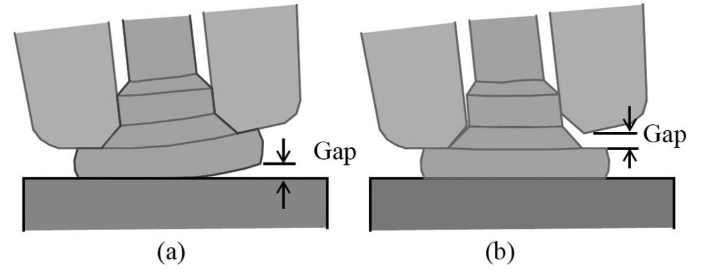

Fig. 13. Illustrations of gaps occurring during ball bonding: (a) at interface before bond completion and (b) at interface between capillary tip and bonded ball, after bond completion. Deformations not to scale.

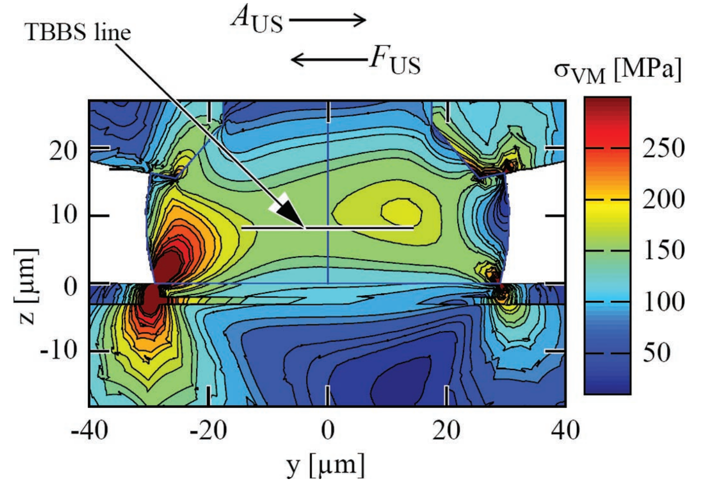

Fig. 14. Simulated von Mises stress in bonded ball and adjacent structures due to ultrasonic and normal forces. Plasticity and interfacial sliding ignored; $x = 0$ and $A_{\mathrm{US}} = 0.599$ μm.

tip and top of the deformed ball. This gap is illustrated in Fig. 13(b). The difference between experiment and simulation is that the experimental gaps reduce stress in their vicinity, and this is compensated for by higher than simulated stress on the alternate half-cycle ($\sigma_z < 0$ region of IFA).

5) Ultrasonic Stress Field in Deformed Ball: Because the model neither includes plasticity nor interfacial slip, the modeled ball acts on the pad similarly to a "frictionless punch" [32]. Thus, the stress fields at the interface edges are bound neither by sliding friction nor plasticity effects in this model. This limitation is considered for the discussion.

The colors in Figs. 11(a) and (b) give information about the von Mises stress σ_{VM} caused by $F_{\mathrm{US}}^{\mathrm{sim}}$ only. The σ_{VM} stress field caused by F_{US} and F_{N} combined is shown in Fig. 14. The yield stress of the bonded ball is estimated to be that of massively deformed and work-hardened Au and is not known. If σ_{Y} is assumed to be 200 MPa, the major part of the bonded ball has σ_{VM} levels below σ_{Y}. The edge portions that point in US direction show $\sigma_{\mathrm{VM}} > \sigma_{\mathrm{Y}}$ once during each cycle. It is expected that these portions yield a few nanometers during several ultrasonic cycles until σ_{VM} on the new geometry falls below σ_{Y}. The small amount expected for this yielding cannot be observed in the experiment [26], because the amount of US-induced ball deformation is not significant with respect to the measurement error. Such nanoscopic yielding is not covered by the simulation, and therefore the stresses calculated very close (a few microns) to the interface edge points ($x = 0$, $y = \pm$ BDI/2, $z = 0$) are higher than those expected in the real application. However, the further away the stresses are calculated the higher their accuracy due to Saint-Venant's principle, which states that stresses

far from where the load is applied do not depend on the actual type of loading [33].

A typical bonded ball bulk stress value (TBBS) is evaluated from the data in Fig. 14. The TBBS is defined as the average von Mises stress on the line BDI/2 $> y >$ −BDI/2 at $z =$ BH/2 and $x = 0$ (TBBS line). The TBBS can serve to indicate if additional deformation (e.g., ultrasonic enhanced deformation) results from the values of F_{US} and F_{N} applied. The resulting value for TBBS is 172 MPa.

6) Ultrasonic Stress Field Under the Pad: Stresses need to be low enough not to fracture any of the CMOS layers or the bulk Si and low enough not to cause interfacial delamination. As an example, the stresses in the underpad bulk Si are evaluated here. If the mechanical stress is too high, Si experiences brittle fracture according to, e.g., the maximum normal stress theory [34]. This theory predicts failure if $\sigma_{\mathrm{t}} \leq \sigma_1$ or $\sigma_{\mathrm{c}} \leq |\sigma_3|$ where σ_{t} and σ_{c} are the tensile and compressive uniaxial yield stress limits (tensile and compressive strengths), respectively, and σ_1, σ_2, and σ_3 are the principal stresses at a given point, in this case ordered such that $\sigma_1 \geq \sigma_2 \geq \sigma_3$. For Si, the maximum possible yield stress is 7 GPa whereas the practical limit can be 33× lower (≈ 200 MPa) due to stress concentration on defects [35]. The bulk material of Si chips has few stress concentrating defects and therefore has a relatively high effective tensile strength. The compressive strength is estimated even higher than the tensile strength.

Simulated principal stresses are evaluated under the dielectric/Si interface at $z = -3.1$ μm (with respect to the origin at the interface) for lines $x = 0$ and $y = 0$ and shown in Figs. 15(a) and (b) for US and bond force combined and for US only, respectively. The simulated maximum principal stress for the combined case is $\sigma_{\max} \approx 275$ MPa (σ_3). Due to the gaps expected at the IFA or capillary/ball interface, the effective $\sigma_{\max}$ is lower than simulated. On the compressive side, the principal stress minimum $\sigma_{\min} = -480$ MPa is that of σ_3 and located at $y = -28.9$ μm under the interface edge. Due to the gaps, the effective $\sigma_{\min}$ is expected even lower than simulated, because the compressive side compensates for the tensile stress missing due to the gaps. Although having a magnitude possibly larger than the simulated $\sigma_{\min}$, the effective $\sigma_{\min}$ in the experimental process does not cause any noticeable defect.

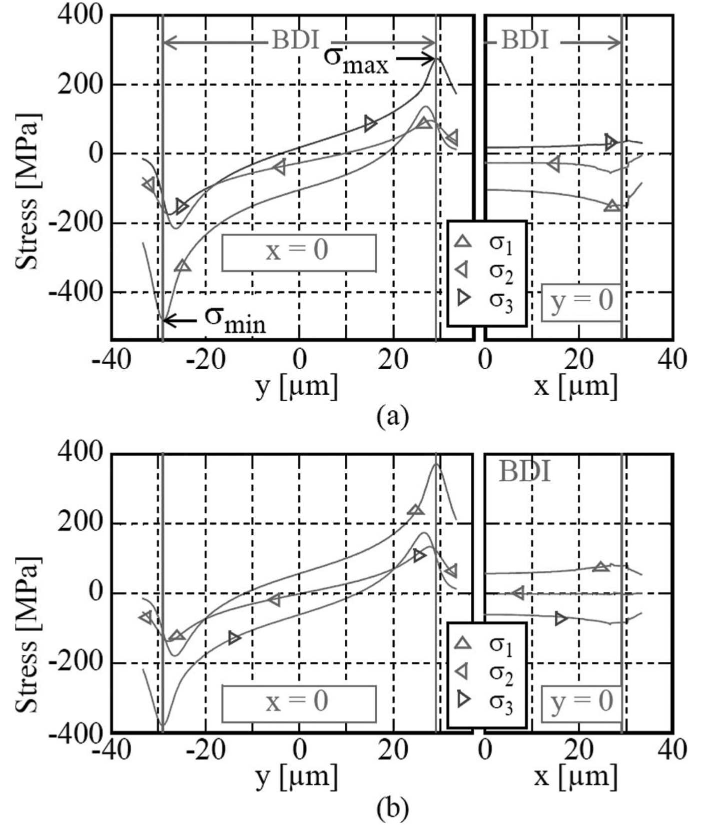

Fig. 15. Principal stresses in underpad Si at $z = -3.1$ μm due to (a) US and bond force combined and (b) US only.

IV. Effect of Capillary Dynamics

A. Comparison Models

Model $\mathrm{U_{dynamic}}$ is compared with 2 modified models, $\mathrm{U_{static}}$ and $\mathrm{U_{stiff}}$, which are both excluding dynamic capillary effects in the ultrasonic range. Model $\mathrm{U_{static}}$ corresponds to model $\mathrm{U_{dynamic}}$ except for the ultrasonic vibration frequency that has been put to 1 Hz, resulting in quasistatic bending. The δ_{z} boundary condition is ignored for simplicity. Only y-displacement A_{y} comparable to A_{US} is applied together with fixing the adhesive bottom. Model $\mathrm{U_{stiff}}$ is the same as $\mathrm{U_{static}}$ except for the capillary elastic modulus that has been put to a value 10^9 times higher. This almost infinitely stiff capillary is very similar to a "hard" capillary tip boundary condition of Dirichlet type that is pushing the bonded ball in ultrasonic direction. In model $\mathrm{U_{stiff}}$, the value of A_{y} virtually does not change along most of the capillary and is less than 2% reduced at the tip.

The nominal values used for A_{y} are adjusted to give an interfacial tangential force F_{T} equal to the value of $F_{\mathrm{US}}^{\mathrm{exp}}$ given in (9). The adjustment is performed using a correction factor $f_{\mathrm{adj}} = F_{\mathrm{US}}^{\mathrm{exp}}/F_{\mathrm{T}}$ where F_{T} is the value obtained when using the original value of A_{y}. The adjusted values of A_{y} are calculated by multiplying the nominal values of A_{y} with f_{adj}. The values of f_{adj} are −2.68 and −0.193 for models $\mathrm{U_{static}}$ and $\mathrm{U_{stiff}}$, respectively.

B. Dynamic Vibration Shape

Ultrasonic vibration shapes for models $\mathrm{U_{static}}$ and $\mathrm{U_{stiff}}$ are given in Figs. 16(a) and (b), respectively, and are compared with that of model $\mathrm{U_{dynamic}}$ (Fig. 11). Although no vibration node is observed along the capillary in model $\mathrm{U_{static}}$, the amount of capillary tip inclination at the ball location is comparable to that observed in model $\mathrm{U_{dynamic}}$. However, model $\mathrm{U_{stiff}}$ has no capillary deformation. Subsequently, the ball deformation largely lacks the z-component. This has a large effect on the stress fields

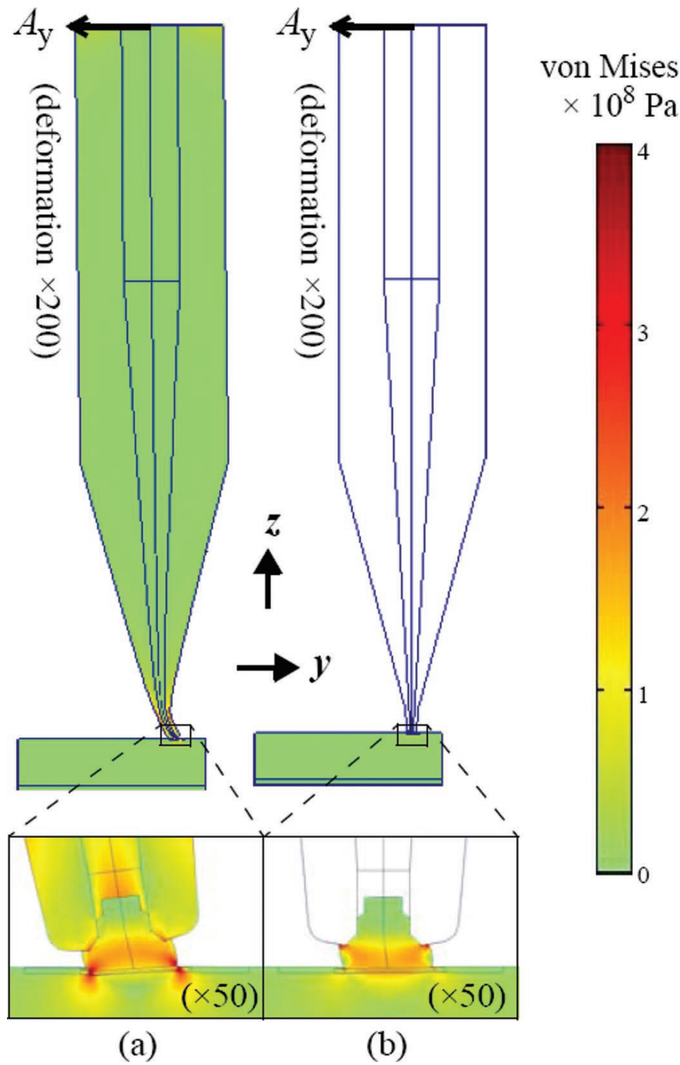

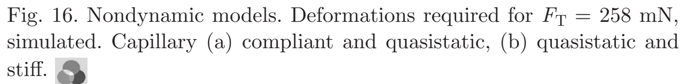
Fig. 16. Nondynamic models. Deformations required for $F_T = 258$ mN, simulated. Capillary (a) compliant and quasistatic, (b) quasistatic and stiff.

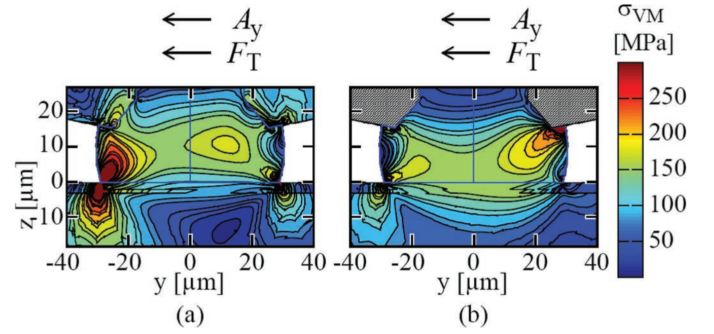

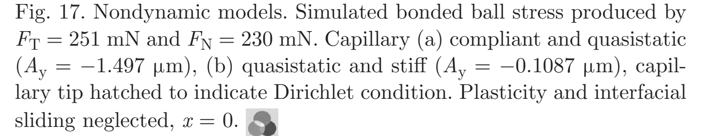
Fig. 17. Nondynamic models. Simulated bonded ball stress produced by $F_T = 251$ mN and $F_N = 230$ mN. Capillary (a) compliant and quasistatic ($A_y = -1.497$ μm), (b) quasistatic and stiff ($A_y = -0.1087$ μm), capillary tip hatched to indicate Dirichlet condition. Plasticity and interfacial sliding neglected, $x = 0$.

as pointed out in the subsections that follow. Compared with model $U_{dynamic}$, the line fraction l_t is slightly larger in model U_{static} and almost negligible in model U_{stiff}, as shown in Table V together with the adjusted boundary conditions and other values explained later. This indicates that the inclination effect is largely due to the capillary compliance.

C. Dynamic Stress in Bonded Ball

The von Mises stress σ_{VM} obtained after superposing the stress fields of $F_T = 251$ mN and $F_N = 230$ mN is shown in Figs. 17(a) and (b) for models U_{static} and U_{stiff}, respectively. The results for U_{static} are very similar to those of $U_{dynamic}$ (Fig. 14). However, the results for U_{stiff} differ considerably because the torque generated in model U_{stiff} causes compressive σ_z on the $+y$ side, adding to the F_N-induced stress, and tensile σ_z on the $-y$ side, compensating for the F_N-induced stress. Thus, model U_{stiff} shows the maximum σ_{VM} in the ($y = +\mathrm{BDI}/2$, $z = \mathrm{BH}$) corner, opposite to where the maxima in models $U_{dynamic}$ and U_{static} are located. The latter maxima are largely determined by the inclination effect stress, being located in the ($y = -\mathrm{BDI}/2$, $z = 0$) corner. The TBBS values are shown in Table V and indicated that models $U_{dynamic}$ and U_{static} are very similar, while the TBBS of model U_{stiff} is 8.1% smaller.

D. Dynamic Underpad Stress

Underpad stresses are determined, shown in Fig. 18 and compared with those from model $U_{dynamic}$; see Fig. 15(a). Again, the results for U_{static} are very similar to those of $U_{dynamic}$. In the presented model, appropriately adjusted boundary conditions make U_{static} useful to get practically the same results as with $U_{dynamic}$. The results for U_{stiff} show considerably lower stress levels. The minimum principal stress values σ_{min} are compared in Table V. The values of σ_{min} for U_{static} and U_{stiff} are 5.4% higher and 43% lower than that of $U_{dynamic}$, respectively. The difference in σ_{min} for U_{stiff} to $U_{dynamic}$ is substantial and expected to change if the model parameters are altered. Therefore, ignoring ultrasonic dynamics in FE modeling of ultrasonic wire bonding [3], [4], [6] will compromise the stress results.

TABLE V. Dynamic Effect of Capillary: Comparison of Models.

Result/Model	$U_{dynamic}$	U_{static}	U_{stiff}
Boundary condition at TSA [μm] (A_y or A_{US})	0.599	−1.497	−0.1087
Line fraction $\sigma_z > 0$:l_t	0.24	0.27	0.01
TBBS [MPa]	172	173	158
σ_{min} [MPa]	−480	−506	−275
y coordinate of σ_{min} [μm]	−28.9	−28.9	−29.5

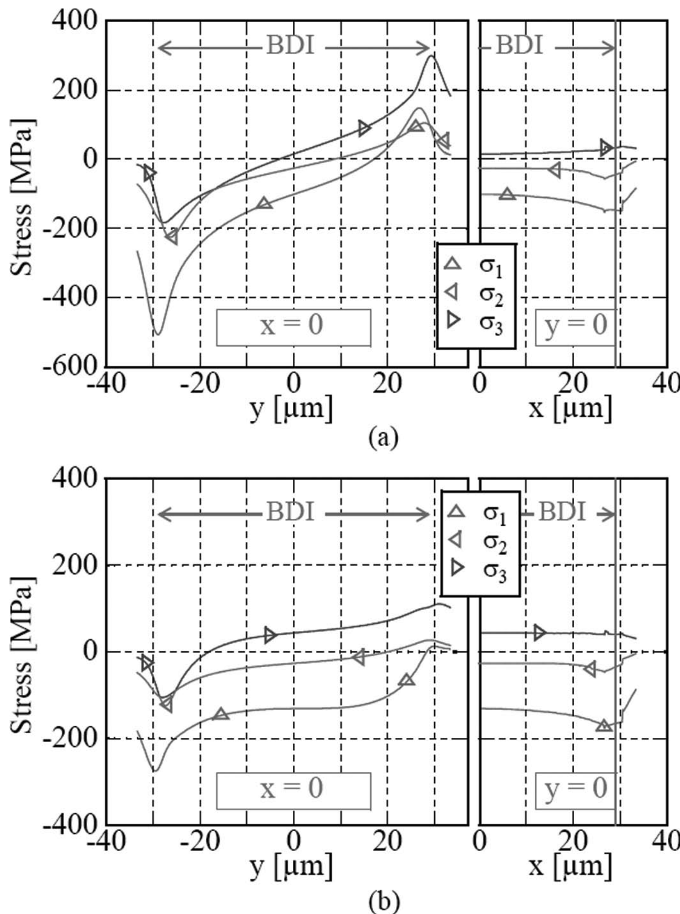

Fig. 18. Principal stresses in underpad Si ($z = -3.1$ µm). Models (a) U_{static} and (b) U_{stiff}.

The inclusion of ultrasonic dynamics is recommended for future optimization studies.

V. Conclusions

A frequency response study of the ball bond/chip/capillary system has been established and includes the effects of the ultrasonic capillary dynamics. A set of quantities was defined that was found to be characteristic for the bonding process. It was studied how the characteristic quantities depend on including the dynamic properties into the simulation. In case ultrasound is ignored, the boundary condition can be adjusted to give the correct value of ultrasonic tangential force. The calculated stress fields resulting from this are only slightly off target. If the static bending effect of the capillary is ignored, they are substantially off target. Thus, it is suggested that the effect of ultrasonic capillary dynamics should be included in mechanical finite element models of wire bonding or a properly modified static bending capillary model with adjusted boundary conditions is used.

The methodology presented allows for a more effective comparison of ball-bonding processes with varying material parameters and geometrical dimensions of the capillary, ball, pad and underpad structure, chip, and die attach adhesive. Processes using different ultrasonic frequencies can also readily be compared with each other.

Acknowledgments

The help of Dr. Dennis Turriff and Mr. Hua Huang for measuring mass density is gratefully acknowledged.

References

[1] G. Harman, *Wire Bonding for Microelectronics—Materials, Processes, Reliability, and Yield*, 2nd ed. New York: McGraw-Hill, 1997.

[2] F. W. Wulff, C. D. Breach, D. Stephan, Saraswati, and K. J. Dittmer, "Characterisation of intermetallic growth in copper and gold ball bonds on aluminum metallisation," in *Proc. 6th Electronic Packaging Technology Conf.*, 2004, pp. 348–353.

[3] L. Zhang, V. Gumaste, A. Poddar, L. Nguyen, and G. Schulze, "Analytical and experimental characterization of bonding over active circuitry," *ASME J. Electron. Pack.*, vol. 129, pp. 391–399, 2007.

[4] J. Schwizer, M. Mayer, and O. Brand, *Force Sensors for Microelectronic Packaging Applications*, Microtechnology and MEMS series. Heidelberg: Springer Science + Business Media, 2005.

[5] C. L. Yeh and Y. S. Lai, "Transient analysis of the impact stage of wirebonding on Cu/low-K wafers," *Microelectron. Rel.*, vol. 45, pp. 371–378 2005.

[6] A. G. K. Viswanath, X. Zhang, V. P. Ganesh, and L. Chun, "Numerical study of gold wire bonding process on Cu/Low-k structures," *IEEE Trans. Adv. Pack.*, vol. 30, pp. 448–456, 2007.

[7] Y. Liu, S. Irving, and T. Luk, "Thermosonic wire bonding process simulation and bond pad over active stress analysis," in *Proc. IEEE Electronic Components and Technology Conf.*, 2004, pp. 383–391.

[8] Y. Takahashi and M. Inoue, "Numerical study of wire bonding—Analysis of interfacial deformation between wire and pad," *ASME J. Electron. Pack.*, vol. 124, pp. 27–36, 2002.

[9] I. Jeon, "The study on failure mechanisms of bond pad metal peeling Part B—Numerical analysis," *Microelectron. Rel.*, vol. 43, pp. 2055–2064, 2003.

[10] Y. Ding, J. K. Kim, and P. Tong, "Numerical analysis of ultrasonic wire bonding: Effects of bonding parameters on contact pressure and frictional energy," *Mech. Mater.*, vol. 38, pp. 11–24, 2006.

[11] C. L. Yeh and Y. S. Lai, "Comprehensive dynamic analysis of wirebonding on Cu/Low-K wafers," *IEEE Trans. Adv. Pack.*, vol. 29, no. 2, pp. 264–270, 2006.

[12] I. Lum, H. Huang, B. Chang, M. Mayer, D. Du, and Y. Zhou, "Effects of superimposed ultrasound on deformation of gold," *J. App. Phy.*, vol. 105, no. 2, art. no. 024905, 2009.

[13] Y. Gao and C. Doumanidis, "Mechanical analysis of ultrasonic bonding for rapid prototyping," *ASME J. Manuf. Sci. Eng.*, vol. 124, pp. 426–434, 2002.

[14] A. Siddiq and E. Ghassemieh, "Thermomechanical analyses of ultrasonic welding process using thermal and acoustic softening effects," *Mech. Mater.*, vol. 40, pp. 982–1000, 2008.

[15] Z. W. Zhong and K. S. Goh, "Investigation of ultrasonic vibrations of wire bonding capillaries," *Microelectron. J.*, vol. 37, pp. 107–113, 2006.

[16] R. G. McKenna and R. L. Mahle, "High impact bonding to improve reliability of VLSI die in plastic packages," in *Proc. Electronic Components Conf.*, 1989, pp. 424–427.

[17] K. Toyozawa, K. Fujita, S. Minamide, and T. Maeda, "Development of copper wire bonding application technology," *IEEE Trans. Comp. Hybr. Manuf. Technol.*, vol. 13, no. 4, pp. 667–672, 1990.

[18] J. Schwizer, M. Mayer, O. Paul, D. Bolliger, and H. Baltes, "Thermosonic ball bonding: Friction model based on integrated microsensor measurements," in *Proc. IEEE/CPMT Int. Electron. Manuf. Tech. Symp.*, 1999, pp. 108–114.

[19] J. L. Harthoorn, "Joint formation in ultrasonic welding compared with fretting phenomena for aluminium," in *Proc. Int. Conf. Ultrasonics*, 1973, pp. 43–51.

[20] J. B. Wachtman and D. G. Lam, "Young's modulus of various refractory materials as a function of temperature," *J. Am. Ceram. Soc.*, vol. 42, no. 5, pp. 254–260, 1959.

[21] M. Shimada, K. Matsushita, S. Kuratani, T. Okamoto, M. Koizumi, K. Tsukuma, and T. Tukidate, "Temperature dependence of Young's modulus and internal friction in alumina, silicon nitride, and partially stabilized zirconia ceramics," *J. Am. Ceram. Soc.*, vol. 67, no. 2, pp. C23–C24, 1984.

[22] R. M. Spriggs, "Expression for effect of porosity on elastic modulus of polycrystalline refractory materials, particularly aluminum oxide," *J. Am. Ceram. Soc.*, vol. 44, no. 12, pp. 628–629, 1961.

[23] F. P. Knudsen, "Effect of porosity on Young's modulus of alumina," *J. Am. Ceram. Soc.*, vol. 45, no. 2, pp. 94–95, 1961.

[24] B. J. Lazan, *Damping of Materials and Members in Structural Mechanics.* Oxford: Pergamon Press, 1968.

[25] A. Wolfenden, "Measurement and analysis of elastic and anelastic properties of alumina and silicon carbide," *J. Mater. Sci.*, vol. 32, pp. 2275–2282, 1997.

[26] A. Shah, M. Mayer, N. Zhou, S. J. Hong, and J. T. Moon, "In situ ultrasonic force signals during low-temperature thermosonic copper wire bonding," *Microelectron. Eng.*, vol. 85, pp. 1851–1857, 2008.

[27] J. Lee, M. Mayer, Y. Zhou, and J. Persic, "Microelectronic wire bonding with insulated Au wire: Effects of process parameters on insulation removal and crescent bonding," *Mater. Trans.*, vol. 49, no. 10, pp. 2347–2353, 2008.

[28] M. Mayer and J. Schwizer, "Microelectronic bonding processes monitored by integrated sensors," in *Sensors Update*, vol. 11, Weinheim: Wiley-VCH, 2002, pp. 219–277.

[29] A. Shah, M. Mayer, Y. Zhou, S. J. Hong, and J. T. Moon, "Reduction of underpad stress during thermosonic copper ball bonding," in *Proc. IEEE Electronic Components Technology Conf.*, 2008, pp. 2123–2130.

[30] A. Shah, M. Mayer, Y. Zhou, S. J. Hong, and J. T. Moon, "Low-stress thermosonic copper ball bonding," *IEEE Trans. Electron. Packag. Manuf.*, vol. 32, no. 3, pp. 176–184, 2009.

[31] M. Mayer and A. Zwart, "Ultrasonic friction power in microelectronic wire bonding," *Mat. Sci. Forum,* vol. 539–543, 2007, pp. 3920–3925.

[32] K. L. Johnson, *Contact Mechanics.* Cambridge: Cambridge University Press, 1987.

[33] A. C. Fischer-Cripps, *Introduction to Contact Mechanics*, 2nd ed. Heidelberg: Springer, 2007, p. 24.

[34] E. P. Popov, *Introduction to Mechanics of Solids.* Upper Saddle River, NJ: Prentice-Hall, 1968.

[35] K. E. Petersen, "Silicon as a mechanical material," *Proc. IEEE*, vol. 70, no. 5, pp. 420–457, 1982.

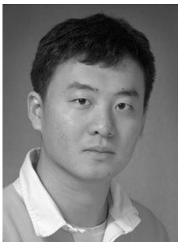

Yan Huang received his B.S. degree with honours in electrical engineering (2007) and an M.S. degree in mechanical engineering (2009) from the University of Waterloo, Ontario, Canada. He is currently with Bell Canada, Toronto, Ontario, Canada.

Aashish Shah received his B.Tech. degree in 2002 from Jawaharlal Nehru Technological University, Hyderabad, India, and M.S. degree in 2006 from the University of Ottawa, Ontario, Canada. He is currently pursuing his Ph.D. degree in the Department of Mechanical and Mechatronics Engineering at the University of Waterloo, Ontario, Canada. His research interests include the study of process and bonding mechanisms in microelectronic wire bonding process using integrated CMOS microsensors. Currently, he is working toward developing novel low-stress copper ball-bonding processes, which minimize the risk of damage to the silicon chip.

Michael Mayer received his diploma degree in physics in 1994 and Ph.D. degree in technical sciences in 2000, both from ETH Zurich, Switzerland, developing a novel family of CMOS microsensors for real-time feedback during the thermosonic ball-bonding process. For his thesis, he was awarded the ETH Medal in 2001. From 2000 to 2004, he was a senior R&D engineer with Esec, Cham, Switzerland. Dr. Mayer has coauthored more than 60 technical publications, including patent applications, a book and several book chapters, and journal and conference papers. He joined the faculty of the University of Waterloo, Ontario, Canada, in 2004.

Y. Norman Zhou received his B.S. and M.S. degrees from the Department of Mechanical Engineering, Tsinghua University, Beijing, China, and Ph.D. degree from the Department of Metallurgy and Materials Science, University of Toronto, Toronto, Canada. He worked as a lecturer at the Department of Mechanical Engineering, Tsinghua University and as a materials scientist at the Fuel Development Branch, Atomic Energy of Canada, Ltd, Chalk River, Ontario, Canada. He also worked as a senior research engineer at the Microjoining and Plastics Group at the Edison Welding Institute, Columbus, Ohio. Dr. Zhou, currently a holder of Canada Research Chair in Microjoining (www.chairs.gc.ca), is also professor at the Department of Mechanical and Mechatronics Engineering, University of Waterloo (www.mme.uwaterloo.ca). He has more than 20 years industrial, teaching, and research experience in materials joining technologies. His current research interests include the field of microjoining and nanojoining (e.g., wire bonding, resistance and laser microwelding, and brazing and soldering).

John Persic photograph and biography not available at time of publication.